Combustion and Flame 256 (2023) 112955

Contents lists available at ScienceDirect

Combustion and Flame

journal homepage: www.elsevier.com/locate/combustflame

Wall heat loss effect on the emission characteristics of ammonia swirling flames in a model gas turbine combustor

Meng Zhang[a,*], Wanying Xu[a], Ruixiang Wang[a], Xutao Wei[a], Jinhua Wang[a], Zuohua Huang[a], Houzhang Tan[b]

[a] State Key Laboratory of Multiphase Flow in Power Engineering, Xi'an Jiaotong University, Xi'an 710049, China
[b] MOE Key Laboratory of Thermo-Fluid Science and Engineering, Xi'an Jiaotong University, Xi'an 710049, China

ARTICLE INFO

Article history:
Received 14 February 2023
Revised 6 July 2023
Accepted 15 July 2023

Keywords:
Ammonia
Flame wall interaction
Wall heat loss
NOx emission
Swirl flames

ABSTRACT

Ammonia (NH_3) combustion is regarded as one of the most promising solutions to realize zero CO_2 emission. However, its low reactivity, low heat release result in a strong thermal effect (wall heat loss effect) which significantly affects flame macro structure and NOx emission characteristics. In this study, an air film cooling on the swirling combustion chamber was designed to investigate the wall heat loss effect on NOx emission. The flame structure and NO production were measured with the OH-/NO-PLIF techniques. The NOx emission was analyzed by the Gasmet DX4000 Fourier Transform Infrared (FTIR) gas analyzer. Large eddy simulation was also conducted with detailed chemistry to extend the understanding of the experimental findings. For the current combustion chamber, a larger convection heat loss was obtained when increasing the cooling air flow rate. NO emission shows a decreasing trend with heat loss which is mainly caused by the chemical reactions at near all region. This can be verified by the relatively farther NO profile from the combustor wall. By analyzing the LES results at near all region, the combustion efficiency is decreased due the lower temperature. As a result, NO production from HNO and NH pathway is suppressed due to the local OH decreasing in near-wall region. The larger unburned NH_3 in the exhausted gas may also consumes NO by the NO reduction reactions. In comparison, N_2O, around 300 times global warming potential than that of CO_2, significantly increases as the heat loss increases. This is mainly because that the production of N_2O from NO is promoted and N_2O decomposition is suppressed within the thermal boundary. This study suggests that N_2O might become a more serious emission component in NH_3 fueled gas turbines. Furthermore, the heat loss effect on the NOx production should be fully considered when designing the gas turbine combustion chamber with strong wall cooling.

1. Introduction

Ammonia (NH_3) combustion is regarded as one of the most promising solutions to realize zero carbon dioxide (CO_2) for the power plants and has been extensively investigated recently [1–6]. The large scale utilization of ammonia in power plants can not only reduce the greenhouse effect but also alleviate the energy crisis [1,2]. As an industrial chemical feedstock, there are mature systems for ammonia production, storage, transportation as well as distribution [2], which is a very good prerequisite. Therefore, replacing fossil fuel with ammonia in modern power systems, such as gas turbines, becomes one of the main objectives for the ammonia research community [1,2]. However, the researches on solving the major challenges of ammonia combustion still have a long way to go. One issue is the flame stabilization caused by the slow flame speed (low reactivity), i.e., the maximum value is 7 cm/s at 298 K and 0.1 MPa [7,8]. The other one is the high fuel NOx emission owing to the high content of nitrogen atom in its molecule (NH_3) [9].

In the practical combustion device, the flame is limited within the combustion chamber which results in a strong flame-wall interaction (FWI). Due to the low chemical reactivity and high sensitivity to heat loss [10,11], FWI will be more distinct for ammonia combustion. FWI mainly consists of: 1) the physical effect; Due to the existence of chamber wall, the recirculation zone (RZ) and shear layer (SL) will be formed, showing an effect on flame stabilization [12]. Moreover, the structure of RZ and SL depends on the fuel properties, i.e., the flame speed and the resistance to strain. In the chamber, both RZ and SL can be further divided into two regions, including inner recirculation zone (IRZ), outer recirculation zone (ORZ), the inner shear layer (ISL) and outer shear layer

---

* Corresponding author.
E-mail address: mengz8851@xjtu.edu.cn (M. Zhang).

https://doi.org/10.1016/j.combustflame.2023.112955
0010-2180/

(OSL) [3]. For example, NH_3/air flame is mainly stabilized in SL region while CH_4/air flame is stabilized in the SL region and outer recirculation zone (ORZ) at $\phi = 0.8$ due to the difference in flame properties [3]; 2) the thermal effect. There will be a strong wall cooling on the practical combustion chamber by the bypass air to reduce the thermal stress, which will highly influence the flame structure as well as the emissions [13]. The convection heat loss through the chamber wall might be comparable with the heat release from the combustion for NH_3/air flame. Therefore, a strong thermal effect will occur due to its low chemical reactivity and low heat release rate resulted from its thicker thermal boundary and larger quenching distance [14,15]. This issue has not been fully recognized since the studies on ammonia combustion were not widely conducted until recently years. In addition, the emerged investigations on ammonia combustion were on the flame stabilization and NOx emission characteristics [3–6,16].

Chamber wall heat loss will decrease the near wall temperature, as a consequence, affecting fuel consumption rate and the chemical pathway of emission production. The investigation of Nakamura et al. [10] demonstrates that there is a more distinct radiation heat loss effect on the laminar flame speed for NH_3/air flame compared with CH_4/air flame. Moreover, the NOx production is also modified due to the flame temperature decreasing caused by heat loss. Even in the swirl flame, the flame macrostructure and the main emission are also highly influenced by wall heat loss [17]. This implies that chamber wall heat loss on ammonia combustion is non-negligible and should be fully considered in combustion chamber design.

Though there are studies conducted on the flame stabilization for NH_3/air swirling flames [2,4–6,18], the work on the effect of wall heat loss on the NOx production and global NOx emission is extremely limited. Nakamura et al. [10] studied the radiative heat loss on the laminar flame speed S_L of NH_3/air flames with one-dimensional simulation. The results show that the minimal relative error of S_L between the adiabatic and radiative conditions is 3% within the equivalence ratio range from 0.7 to 1.3. In comparison, it is below 1.5% for CH_4/air flame at the same equivalence ratio range. Furthermore, lower NO concentration at post flame is observed for lean combustion of $\phi < 0.8$ and rich combustion of $\phi > 1.1$ when the heat loss is considered. Lee et al. [19] examined the cool flame ignition and stabilization on heated walls with different surface reactivities. The results showed that significant wall chemical effects occur during the cool flame ignition process. Hayakawa et al. [20] studied the product gas and N_2O emission characteristics of premixed NH_3/H_2/air flames with a laminar stagnation flow. They addressed the relationship of N_2O with the flame temperature downstream of the reaction zone. Results show that heat loss to the stagnation wall significantly affects the behaviour of product gas and N_2O. Okafor et al. [17] demonstrates that the wall heat loss is also non-negligible for swirling flames, even at a thermal power magnitude of 10 kW. They found the flame front is farther from chamber wall when applying uninsulated square-shaped liner, indicating there exists local quenching caused by wall heat loss. The wall heat loss also causes significant reducing in NO emission, which was verified through the 3D large eddy simulation (LES) by Somarathne et al. [21]. Moreover, the N_2O emission, which shows a greenhouse effect about 300 times larger than CO_2, increases to a considerable level. This issue was also found and analyzed in the investigations of by Mashruk et al. [22,23]. In the study of Okafor et al. [17], the wall heat loss was mainly controlled through the application of heat insulation on the combustor walls. In the other words, heat loss was mainly caused by the natural convection between the chamber outer wall and ambient air. However, in gas turbines chamber wall heat loss is mainly caused by convection, which resulted from the bypass air. The investigation on the NOx emission behaviour with gradually increasing convection heat loss has not been conducted yet.

Based on the above consideration, the objective of this study is to investigate the wall heat loss on the NOx emission characteristics of ammonia combustion in a model swirling combustor. An air film cooling was designed to control the wall convection heat loss. Planar Laser Induced Fluorescence (PLIF) technique was utilized to detect the instantaneous flame macrostructure and the local species concentration NO. Fourier Transform Infrared (FTIR) spectrometry was employed to measure NOx emission at different heat loss condition. Lastly, LES with a dynamic thickened flame model (DTF) based on OpenFOAM was performed to comprehensively analyzing NOx production and consumption mechanisms.

2. Experimental setup and numerical methodology

2.1. Experimental setup

The experiment was conducted with a formerly used fully premixed swirl combustor with the chamber inner dimension of $75 \times 75 \times 180$ mm^3, as introduced in [3,24]. The schematic structure of the combustor, the chamber as well as the swirler are shown in Fig. 1(a). A copper swirler with 12 vanes was used to produce swirl flow with the swirl number of $S = 0.72$, see Fig. 1(a). The parameters for the swirler are $\theta = 45^\circ$, $D_i = 18$ mm and $D_o = 35$ mm. To further confine the flame, a contraction section was mounted at the chamber outlet. The side wall cooling was performed through an air film which was supplied from the bottom outside the chamber, mimicking the bypass air cooling out the gas turbine chamber, as shown in Fig. 1(b). The quartz glass walls were applied to allow the laser diagnostics. For the conditions applying air filming cooling, the air with normal temperature was supplied to four side walls to ensure an even cooling effect for each side. The wall temperature was measured by thermocouples at different downstream locations with the assumption of a axisymmetric flame, as shown in Fig. 1(a) and (b). Then the quantity of the wall convection heat loss can be evaluated through the temperature difference between the flame and chamber wall. By taking this measure, the heat loss can be adjusted through the flow rate of cooling air, Q_{cooling}. The measured temperature profile can be used to define the heat loss or provide the thermal boundary to LES simulation. For the global NOx emission measurement, a new sampling probe was designed as shown in Fig. 1(b). The sample gas was pumped from all sides at the converged section to eliminate the spatial differences. Gaseous ammonia (purity > 99%) was injected in the throat position to fully premix fuel and air, see Fig. 1(a). The flow rates of ammonia and air were controlled using mass flowmeters (CS200 and CS330, SevenStar Co., Beijing China) with accuracies ranging from ±1.0% to ±1.5% of the full scale. Figure 1(c) shows the computational domain of the chamber as well as the measurement windows, the positions of the laser diagnostics. The coordinate system in Fig. 1(b) and (c) helps to refer the measurement and numerical positions and will be used in the rest of the paper.

2.2. The laser diagnostics

The instantaneous OH and NO species profiles were measured with OH/NO Plane Laser Induced Florescence technique (abbreviated as OH-PLIF and NO-PLIF) in multiple measurement planes, namely at $x = 0$, 15, 25 mm, as shown in Fig. 1(c). The system mainly consists of a Q-smart 1500 YAG laser (10-Hz repetition rate), a Q-scan dye laser (Quantel Laser Inc.) and an Andor iStar ICMOS camera. For OH-PLIF measurement, a 10 Hz, 532 nm laser was produced by the YAG laser and the laser frequency was doubled and adjusted to 314.410 nm through the dye laser. A laser sheet with 100 mm in height, at the energy of 2 mJ/pulse was

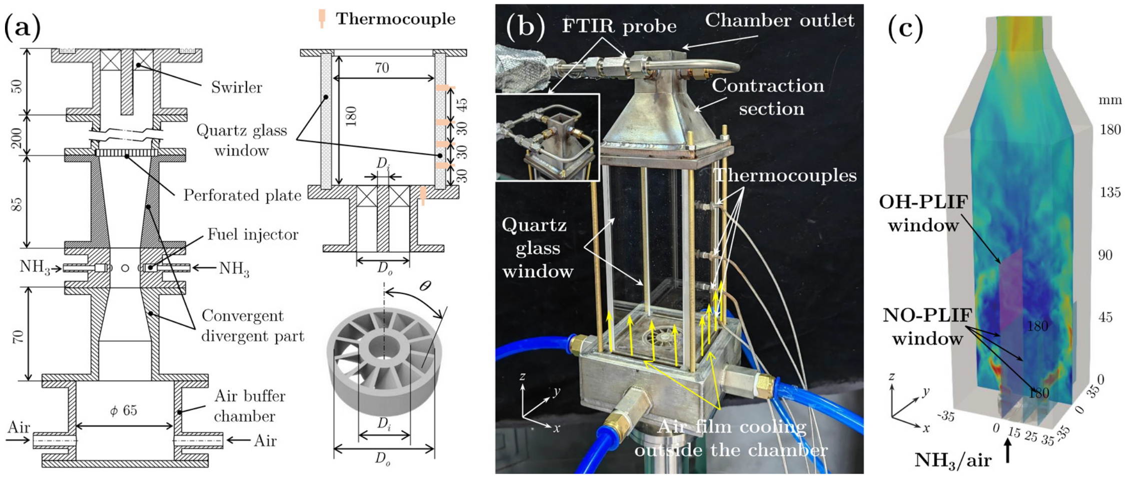

Fig. 1. The burner used in the experiment, where the chamber wall is cooled through the air film cooling. (a) The schematic structure of the combustor, the chamber and the swirler; (b) the direct photo of the combustion chamber; (c) the LES computational domain and the schematic of the OH-PLIF and NO-PLIF measurement window and positions.

formed at the measurement plane. For NO-PLIF, the laser sheet, from the same laser source, was adjusted to 6 mm in height and 6 mJ/pulse at the excitation wavelength 226.074 nm. The OH/NO image was captured with the Andor iStar camera at a frequency of 4 Hz equipped with a UV lens (85 mm, $f/4.5$) and the corresponding band-pass filter for OH and NO fluorescence. The view windows for OH-PLIF and NO-PLIF image were 70 × 105 mm^2 and 70 × 60 mm^2, respectively.

The Partial Image Velocimetry (PIV) was performed to validate the LES results. The system contains a dual-cavity Nd:YAG laser (Litron), a particle generator and a double shutter CCD camera (Imager LX 2M). A laser sheet with 60 mm in height and the thickness of 1 mm was generated with the wavelength of 532 nm, pulse energy of 2 × 300 mJ at 10 Hz. Titanium dioxide (TiO_2), about 0.5 μm in diameter, was selected as the seeding particle. The CCD camera, 1600 × 1200 pixels, was equipped with a macro lens (100 mm, F/2.8) and a narrow bandpass filter (LaVision, 532 ± 5 nm, bandwidth of 10 nm) to capture the Mie scattering signal.

2.3. Measurement on the global emissions

The main emissions were measured using the Gasmet DX4000 Fourier Transform Infrared (FTIR) gas analyzer with a Gasmet Portable Sampling System (PSS) with a scanning frequency of 5 Hz, as introduced in our previous studies [25,26]. The sample pump, heated filter and valve were preheated to 453 K (180 °C) before the measurement. To avoid the residual gas, the zero point calibration was performed before each series of measurements and the data was logged no less than 180 s after each component approached steady state. The exhaust gas simple probe was mounted in the converged part as introduced in earlier section. Uncertainties for NO and $N_2O(NO_2)$ measurement were less than ±15 ppm and ±8 ppm in this study. The maximum uncertainty for NH_3 was ±30 when the its mole fraction was larger than 500 ppm. The global emission values of each species were taken as the mean value of the collected data.

2.4. The dynamic thinkened flame (DTF) model

Large eddy simulation (LES) with a finite rate chemistry based on open source code OpenFOAM was performed on the same burner geometry as the experiment. LES only resolves the vortex larger than the grid size and simulates the vortex with the subgrid model. When performing LES on premixed combustion, the filter size of LES is usually larger than the thickness of the flame which is about $0.1 \sim 1$ mm. In this study, to resolve the flame structure with a coarse mesh, the flame was artificially thickened by a factor of F while keeping the laminar flame speed S_L unchanged, which is recognized as dynamic thickened flame model (DTF) [27]. A subgrid flame wrinkling factor Ξ_Δ based on fractal theory was included [28] to account for the unresolved flame wrinkling due to the thickening process. The chemical source term and the diffusion term were modified by F and Ξ_Δ. The conservation equation of instantaneous species mass fraction after a LES filter becomes

$$\frac{\partial \bar{\rho}\tilde{Y}_k}{\partial t} + \nabla\left(\bar{\rho}\tilde{\mathbf{U}}\tilde{Y}_k\right) = \nabla \cdot \left(\bar{\rho}F\,\Xi_\Delta D_k \nabla \tilde{Y}_k\right) + \frac{\Xi_\Delta \bar{\dot{\omega}}_k}{F}, \tag{1}$$

where ρ and μ are the density and velocity. Y_k, ω_k and D_k represent the kth species mass fraction, reaction rate and mixture-averaged molecular diffusion coefficient. To consider the diffusivity of every species to kth species, D_k was calculated by:

$$D_k = \frac{1 - x_k}{\sum_{j \neq k}^{N} \left(x_j / D_{jk}\right)}, \tag{2}$$

where x_k is the mole fraction of species k, D_{jk} is the binary diffusion coefficient of species j and k. The dynamic thickened factor F which can thicken both preheat and reaction zones, was calculated by Han et al. [29]:

$$F = 1 + (F_0 - 1)\tanh(\alpha \cdot \Omega). \tag{3}$$

In the above formula, the constant α is a parameter controls the thickness of the transition layer between thickened and non-thickened zones. It further helps to distinguish the hot and cold region. $\alpha = 100$ was applied in the current study [30]. F_0 represents the maximum thickening factor defined by the larger value of 1 and $n_{\mathrm{dtf}}\Delta x/\delta_l^0$. n_{dtf} is the thickening coefficient of global grid and also can be understood as the expected grid points in the flame front. Δx is the grid size. δ_l^0 is the unstretched laminar flame thickness defined by the maximal temperature gradient [31]. Ω is the flame surface probe function and is defined by $\Omega = 16c(1-c)^2$ [30] where c is the progress variable defined by temperature. The probe function determines the position of the flame region and judges the local fluid element inside or outside the flame. In the current study, $\Omega = 1$ ($\Omega = 0$) represents the interior (external) of the flame.

The flame wrinkling factor Ξ_Δ was used to offset the loss of the flame wrinkling after thickening, given by Charlette et al. [28], Wang et al. [32]:

$$\Xi_\Delta = \left\{1 + \min\left[1, \max\left(\frac{\Delta}{\delta_l} - 1, 0\right), \Gamma\left(\frac{\Delta}{\delta_l}, \frac{u'_\Delta}{S_l}, Re_\Delta\right)\frac{u'_\Delta}{S_l}\right]\right\}^{\beta}, \tag{4}$$

where Δ is the filter width, u'_Δ is the subgrid turbulence intensity, Re_Δ is the subgrid Reynolds number, and β is the model coefficient, given by Wang et al. [32,33]:

$$\beta = 1 + \frac{\log\left(\left\langle \widehat{W_{\Delta,k}(\tilde{Q})}\right\rangle / W_{\gamma\Delta,k}(\widehat{\tilde{Q}})\right)}{\log(\gamma)}. \tag{5}$$

The one-dimensional adiabatic unstretched laminar flames were calculated by the ANSYS CHEMKIN-PRO package. Detailed information of DTF model can be found in our previous studies [27].

2.5. Numerical implementation

The convective and diffusion terms were discretized and combined respectively by the second order precision TVD scheme correction. The time term was discretized by the implicit Euler method and PISO method was set to deal with the coupling problem of pressure and velocity in the momentum equation. Dynamic Smagorinsky model was used for subgrid turbulence viscosity modelling. To ensure the stability and accuracy of LES, a fixed time step ($\Delta t = 2e^{-6}$) was used to keep the Courant number lower than 0.1 during the entire calculation.

The computational domain includes the swirler, combustion chamber ($70 \times 70 \times 180$ mm^3) and the contraction section, as shown in Fig. 1(c). The overall computational domain was divided into 274 blocks and contained about 5 million structured grids with a minimum grid spacing of 0.2 mm at the flame location. The flow boundary parameters, such as turbulent intensity, integral scale and the mean velocity just ahead of the swirler were measured with hot-wire anemometer (Dantec, Streamline 90N) experimentally [34], which will be shown in the coming section. To fully capture the flame characters in experiments, the timeVaryingMapped module in OpenFOAM was implemented to generate the same turbulence parameters as experiments at the inlet of the computational domain. To account for different wall heat loss in the current study, the wall temperatures at five locations were measured for different conditions. The measurement locations were shown in Fig. 1(a). Then the isothermal wall boundary condition, taken from the fitting curve of the experimental data, was applied at chamber side walls to mimic the air film cooling effect [21]. The schematic of the thermal boundary conditions applied upon the computational domain is shown in Fig. 2. $T = 293$ K was applied to the bottom wall of the chamber. The surface of the swirler was set adiabatic. The wall temperature of the contraction section was set as the temperature value at $z = 180$ mm. Pressure outlet was applied at the exit of the chamber which was verified adequately by capturing the flow in the combustion chamber [3]. We verified the reacting flow fields with the experimental PIV results and compared the mean numerical NO profiles with the NO-PLIF measurement.

In this work, the zero-dimensional (0D) combustion and one-dimensional (1D) laminar flame were calculated by ANSYS Chemkin-PRO [35]. Both LES and 0D/1D calculations were performed using the chemical mechanism of NH_3/air developed by Stagni et al. [36] with 31 species and 203 reactions. Each LES case requires approximately 0.06 million CPU hours with the current mesh and chemical mechanism.

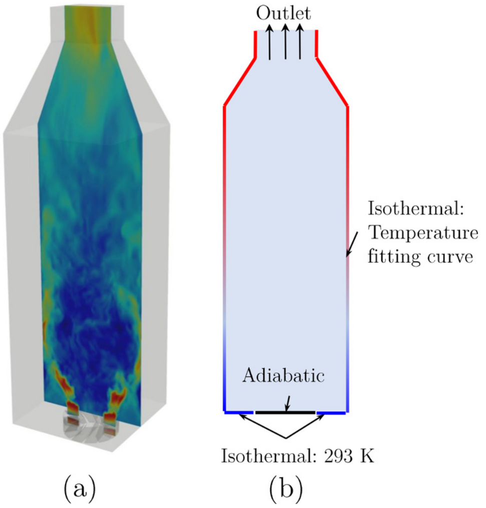

Fig. 2. (a) The computational domain; (b) thermal boundary conditions applied in the simulation.

Table 1
Experimental and numerical operating conditions of the NH_3/air flames in the current study. AC represents the adiabatic condition.

Item	NO-PLIF	OH-PLIF	FTIR	LES
ϕ	0.7–1.1	0.8	0.65–1.15	0.8
U_{in}	10 m/s	10 m/s	10 m/s	3 m/s
$Q_{cooling}$	0, 600, 1200 L/min			AC, 0, 200, 600 L/min
P_w	18.8 kW ~ 22.1 kW			18.8 kW

Table 2
The flame properties in the simulation. n_{dtf} is the number of grid points in the flame front.

Flame	ϕ	T_{ad} (K)	S_L	δ_L	n_{dtf}
NH_3/air flame	0.8	1856.4	4.5	2.3	5

2.6. Operating conditions

The flame tested in this study was the NH_3/air flame. The operating conditions for experimental measurements and LES are listed in Table 1. NO-PLIF, OH-PLIF and FTIR measurements were performed at a fixed chamber inlet velocity of $U_{in} = 10$ m/s with the thermal power of 18.8 kW ~ 22.1 kW. Three air cooling rates of $Q_{cooling} = 0, 600, 1200$ min/L were applied in experiment to mimic different amount of wall convection heat loss. The equivalence ratio range for NO-PLIF measurement was from 0.7 to 1.1 with the ϕ increment of 0.1. OH-PLIF was also performed for comparison purpose at $\phi = 0.8$ and $U_{in} = 10$ m/s. ϕ was ranged from 0.65-1.15 with the increment of 0.05 for the FTIR measurements. LES was performed at $U_{in} = 3$ m/s for the lean condition of $\phi = 0.8$. We simulated the adiabatic condition (AC) and the wall cooling conditions of $Q_{cooling} = 0, 200, 600$ min/L. The flame properties used in LES are listed in Table 2.

3. Results and discussions

3.1. Chamber wall heat loss

To investigate the convection heat loss through combustion chamber wall, the wall temperature was measured at different downstream locations as shown in Fig. 1. In the experiments, the air film cooling outside chamber side walls mimics the by pass air outside the liner in gas turbines. The convection heat flux can be calculated through convection between the bypass air and the

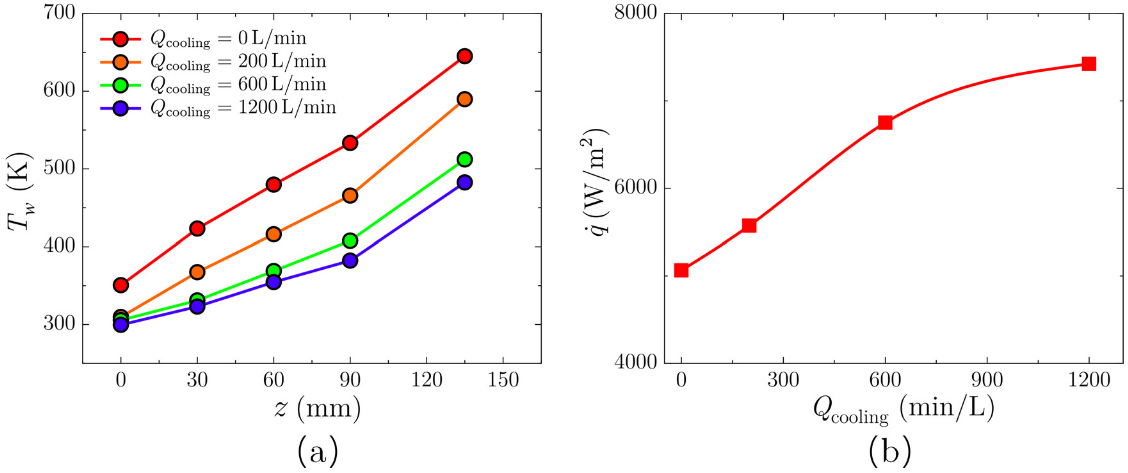

Fig. 3. (a) The measured wall temperatures T_{w} with downstream distance z and (b) the evaluated total heat loss through the chamber wall with Q_{cooling}. The flame was operated at $\phi = 0.8$, $U_{\mathrm{in}} = 10$ m/s at the power of about 18.8 kW.

Table 3
The constants in the convection correlation.

a	b	c	m	n
0.664	1/2	1/3	0.59	0.25

chamber wall by

$$\dot{q}_{\mathrm{conv}} = h_{\mathrm{conv}} \cdot \Delta T. \tag{6}$$

$\dot{q}_{\mathrm{conv}}$ is the heat flux, h_{conv} is the convective heat transfer coefficient. ΔT represents the temperature difference defined as $\Delta T = T_{\mathrm{w}} - T_{\infty}$. T_{w} and T_{∞} are the wall temperature and gas temperature infinity far away, respectively. For the natural convection ($Q_{\mathrm{cooling}} = 0$ L/min), the typical form of the convection correlation can be calculated by

$$Nu = m \cdot (Gr \cdot Pr)^n \tag{7}$$

The above correlation will be Eq. (8) for the forced convection, i.e., $Q_{\mathrm{cooling}} = 200$, 600 L/min.

$$Nu = a \cdot Re^b \cdot Pr^c \tag{8}$$

In above equations, Nu, Re, Gr and Pr represent the dimensionless number of Nusselt number, Reynolds number, Grashof number and Prandtl number. m, n, a, b and c are constants depending on the convection configurations. The four dimensionless parameters and the constants were taken from Ref. [37,38]. For the vertical flat plate, those constants are listed in Table 3. Once the Nusselt number is determined, the convection heat flux can be calculated by Eq. (6), where h can be deduced by

$$\frac{h_{\mathrm{conv}} l}{\lambda} = Nu. \tag{9}$$

λ is the thermal conductivity of the flow, l is the characteristic length of chamber wall. The heat transfer coefficient for radiation can be calculated by Agostinelli et al. [39], Capurso et al. [40]

$$h_{\mathrm{rad}} = \frac{1}{\epsilon\sigma(T_{\mathrm{w}}^4 - T_{\infty}^4)/(T_{\mathrm{w}} - T_{\infty})}. \tag{10}$$

In the current study, a value of $\epsilon = 0.8$ is assumed. σ is the Stefan–Boltzmann constant. Then the total heat loss through the chamber wall can be evaluated by

$$\dot{q} = (h_{\mathrm{conv}} + h_{\mathrm{rad}}) \cdot \Delta T \tag{11}$$

Figure 3 (a) shows the distribution of the measured wall temperature and the total heat loss through the chamber wall. It can be seen that the flame wall temperature T_{w} increases with downstream distance. The lower temperature near the chamber inlet is mainly caused by the cooling effect of the refreshed air in the ORZ. For NH_3/air flame, the flame envelope is long due to the smaller flame speed and the large residence time in the chamber [3]. Therefore, the heat release region can extend to the chamber outlet. This will lead to that the wall heat loss occurs through the entire chamber wall. Moreover, a significant cooling effect is observed when Q_{cooling} is increasing, which can be clearly demonstrated by the temperature decrease at the same downstream location. For example, as Q_{cooling} increased from 0 to 1200 L/min, the wall temperature is decreased from 423.1 K to 323.1 K at $z = 30$ mm. The total heat loss $\dot{q}$ is shown in Fig. 3(b), which is evaluated by Eqs. (6)–(11). It can be observed the heat loss significantly increases when the cooling is strengthened. The averaged value is 5800 W/m^2 for Q_{cooling}= 1200 L/min, which is non-negligible comparing with the heat release from the flame. This also indicates that the air cooling effect is the main contribution to the wall heat loss in the current experimental setup.

3.2. The instantaneous OH/NO profile

To investigate the influence of heat loss on flame structure and NO production, the OH-/NO-PLIF was performed in multiple planes. Figure 4 demonstrates the instantaneous OH-PLIF images of $\phi = 0.8$ at $x = 0$ and 25 mm. To further show the NO profile, the instantaneous NO profiles with ϕ at $Q_{\mathrm{cooling}} = 0$, 600 and 1200 L/min are shown in Fig. 5. The positions of the OH and NO measurement planes are shown Fig. 1(b). According to the theory of the laser diagnostics, the local counts of the single PLIF shot represents the instantaneous species concentration. The laser and ICMOS camera used the same settings for either NO-PLIF or NO-PLIF measurements. Therefore, it can be expected that the local counts of OH/NO-PLIF image represent the instantaneous concentration of OH/NO species and the qualitative comparison can be made for different cases.

When looking at Fig. 4, a clear “V” shape flame is seen at $x = 0$ mm, as discussed in Ref. [3]. The increase of cooling air shows visible effects on OH profile and the flame structure at the center plane ($x = 0$ mm) for all cooling conditions. The wrinkling scales of the flame front, which is indicated by the sharp OH boundary [34,41], seems to be more fragmented when Q_{cooling} is increased. Furthermore, at the measurement plane of $x = 25$ mm, which is closer to chamber wall, the flame structure shows a more fragmented structure and the OH intensity shows a clear decrease

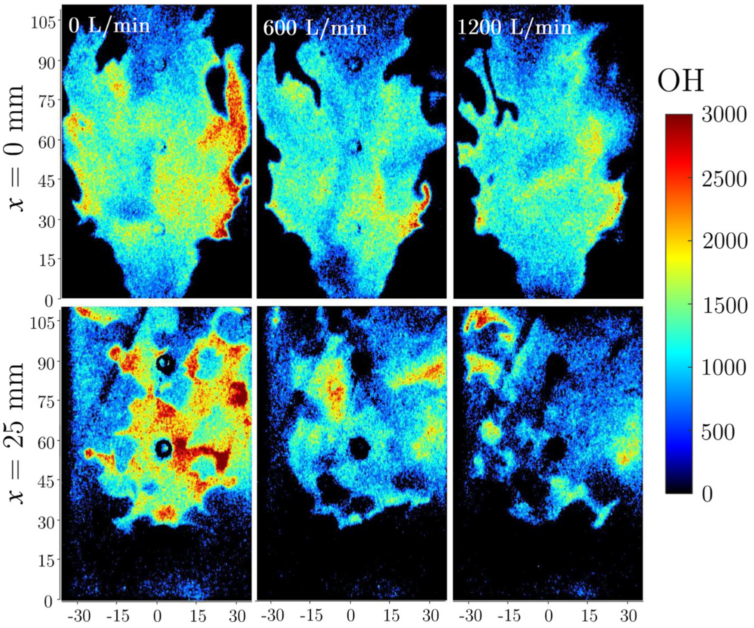

Fig. 4. Instantaneous OH-PLIF images with the cooling air flow rate $Q_{cooling} = 0$, 600 and 1200 L/min. The flame was operated at $\phi = 0.8$ with the mean chamber inlet velocity of $U_{in} = 10$ m/s.

by increasing $Q_{cooling}$. This indicates that the air cooling affects the flame structure near the wall.

To further clarify the flame structure and the NO production of ammonia premixed flames, the NO-PLIF images at $x = 0$ mm are shown in Fig. 5. It can be observed that the NO intensity of the single shot image slightly increases from $\phi = 0.7$ to 0.8 and then shows a clear decreasing trend when ϕ further goes from 0.8 to 1.1. This demonstrates a consistent behaviour as the global NO emission characteristics reported in previous studies [5,26]. For the lean conditions shown in Fig. 5, the flame front, indicated by boundary of NO profile, tends to be relatively farther from the combustor wall due to the enhanced convection heat loss by the cooling air. The distance of the flame front to the chamber wall, mentioned as quenching distance in the literature [14,15], is affected by the relatively thick thermal boundary layer near the wall. Due to the lower heat release rate and high activation energy of ammonia fuel, the wall heat loss will cause combustion intensity and the combustion efficiency to decrease near the wall. As a consequence, the NO production near the wall is suppressed by the low combustion efficiency region since NO mainly comes from the fuel consumption. For flames of $\phi = 1.0$ and 1.1, no visible difference is seen since the NO intensity is too weak. The effect of wall heat loss on the NO-PLIF images is also verified by the global emissions of NO and unburned NH_3, which will be discussed in the following section.

The instantaneous NO profile was also measured in the plane of $x = 25$ mm, as shown in Fig. 6. The images of $\phi = 1.0$ and 1.1 were not shown here because the image intensity is nearly invisible. A slight decrease on NO intensity and the area of NO region can be observed, indicating the NO production rate at near wall region is suppressed with the increase of $Q_{cooling}$. The increase of heat loss thickens the thermal boundary which causes flame local quenching and makes the flame more fragmented near the wall, implying a stronger flame-wall interaction. In summary, the wall convection heat loss through combustion chamber wall highly influence the flame structure and NO species production at near wall region due to the low chemical reactivity within the relatively thick thermal boundary of NH_3/air flame. This effect should be fully considered in the design of NH_3 fuelled gas turbine combustion chamber.

To further quantitatively investigate the instantaneous OH and NO concentration, the time summation of plane-integrated NO-PLIF (OH-PLIF) intensities I_{NO} (I_{OH}) was employed, which is defined as

$$I_{NO} = \sum_{1}^{N} \int I_{local} dA \tag{12}$$

I_{local} represents the local counts of the single shot image and N is the number of the processed images. In the current study, I_{NO} and I_{OH} were averaged from 300 PLIF images. Then, the global OH and NO concentration during the combustion can be denoted by I_{NO} or I_{OH}. Figure 7 shows the variation of the plane-integrated time-averaged OH-PLIF and NO-PLIF intensities with $Q_{cooling}$ at $U_{in} = 10$ m/s and $\phi = 0.8$. In Fig. 7, it is clear that the total counts for both OH and NO barely changes with $Q_{cooling}$ at the symmetrical plane of $x = 0$ mm. However, both NO and OH show an overall decreasing trend as $Q_{cooling}$ at the measurement plane close to the wall of $x = 25$ mm, which further verifies the local quenching and lower combustion efficiency near the wall. It is already recognized that NO is produced through intermediate species HNO resulting from the oxidation of NH_i by O, H and OH radicals [6,26]. Therefore, the decrease of OH and other species near the wall reduce the production of NO. We also plotted I_{NO} at $x = 15$ mm in the figure for comparison. It is seen that the decreasing rate of I_{NO} is larger when the measuring plane is closer to the wall, indicating a larger effect of the wall heat loss.

3.3. Global emission characteristics

In this section, we discuss the global emission characteristics of NO, NO_2, N_2O and unburned NH_3 when the air cooling was applied. To eliminate uncertainties by the ambient air entrainment at burner outlet, a contraction section is mounted in the combustion chamber, see Fig. 1(a). The variations of those emissions with equivalence ratio at different $Q_{cooling}$ are plotted in Fig. 8. As discussed in our previous studies [25,26], fuel-lean ammonia flames are characterized by high NO emission which is more than 1000 ppm at $0.7 < \phi < 1.0$, with the peak at about $\phi = 0.8$. While, the low NO emission, i.e., below 300 ppm, was detected at fuel-rich flames of $1.0 < \phi < 1.1$. This can be verified in Fig. 8(a) at the condition of $Q_{cooling} = 0$ L/min.

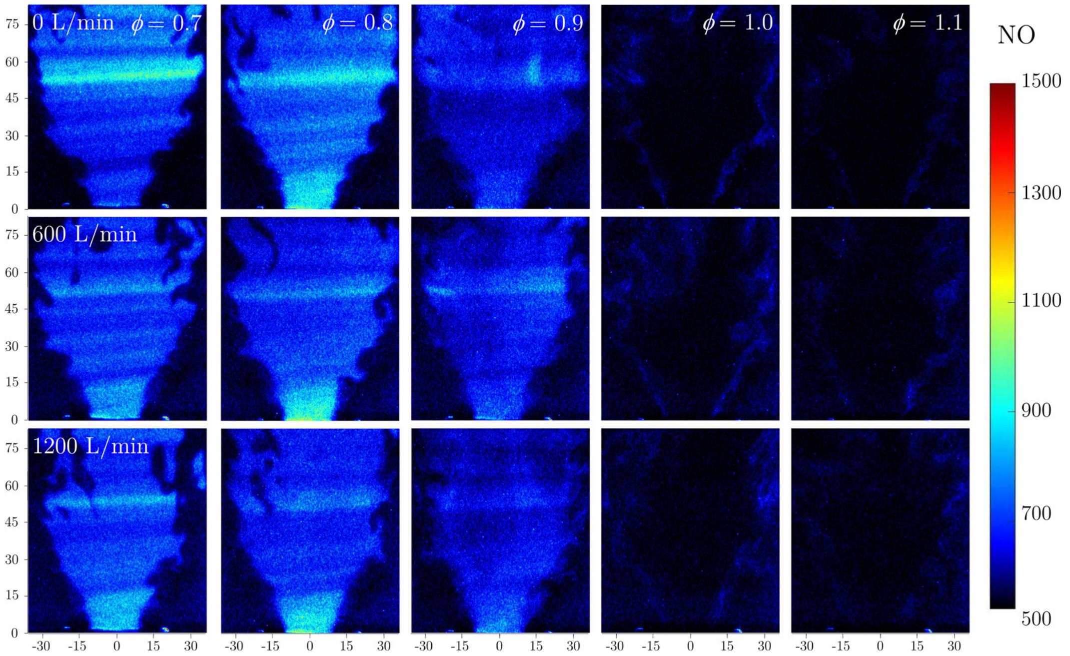

Fig. 5. Instantaneous NO profiles with equivalence ratio ϕ at different cooling air flow rate in the measurement plane of $x = 0$ mm. First row: $Q_{cooling} = 0$ L/min, middle row: $Q_{cooling} = 600$ L/min and bottom row: $Q_{cooling} = 1200$ L/min. The mean chamber inlet velocity was kept at $U_{in} = 10$ m/s. The laser and ICMOS camera used the same settings for NO-PLIF measurements. The local counts on the single NO-PLIF shot represents the instantaneous concentration of NO species.

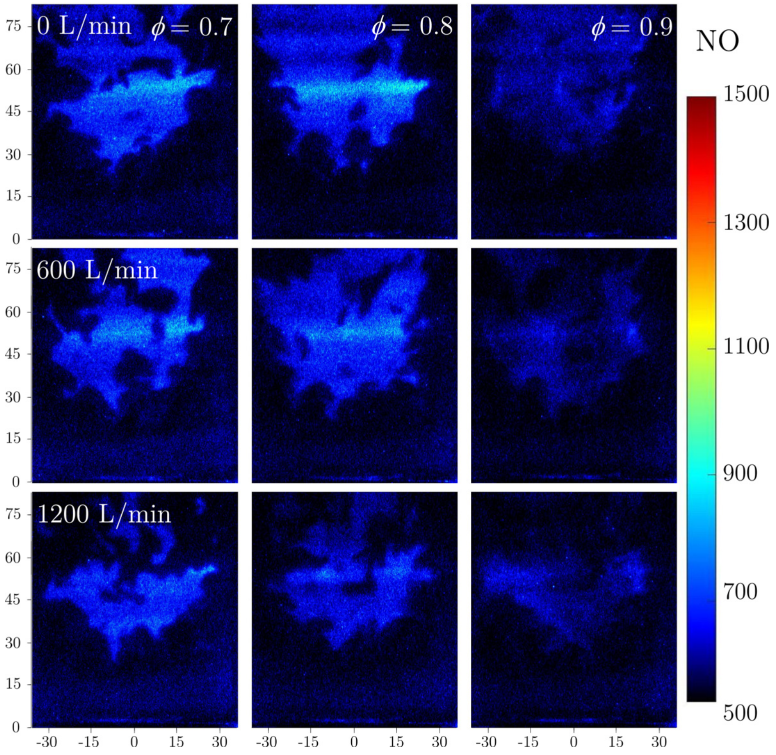

Fig. 6. Instantaneous NO profiles with equivalence ratio ϕ at different cooling air flow rate in the measurement plane of $x = 25$ mm. The NO-PLIF was performed on the same operating conditions corresponding to Fig. 5.

In Fig. 8(a), it is readily seen that NO emission significantly decreases with the cooling air flow rate at fuel-lean conditions. The largest decrease is observed at the NO peak condition corresponding to $\phi = 0.8$. In this case, NO is about 2300 ppm at $Q_{cooling} = 0$ L/min while it is lower than 1200 ppm at the cooling air flow rate of 1200 L/min. According to the analysis on the NO emission of ammonia combustion [10,17], the contribution of OH on NH, HNO and NO production is largely reduced due to the decreased temperature by heat loss. NO production from HNO and NH pathway is suppressed due to the local OH decreasing in near-wall region, which will be discussed in detail by LES results in the last section. On the other hand, the combustion efficiency of NH_3 will be reduced due to the temperature decreasing in near-wall region. As shown in Fig. 8(d), large unburned NH_3 is ob-

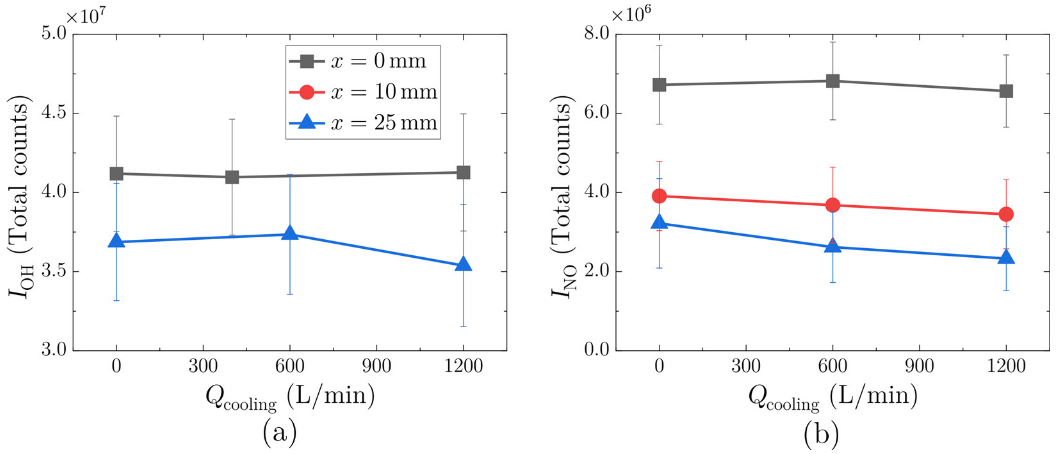

Fig. 7. Variation of the plane-integrated time-averaged OH-PLIF and NO-PLIF intensities with $Q_{cooling}$ at $U_{in} = 10$ m/s and $\phi = 0.8$. The error bars shows the standard deviation calculated from 300 instantaneous shots. OH-PLIF was only conducted for $x = 0$ and 25 mm. The legend are applied for both figures.

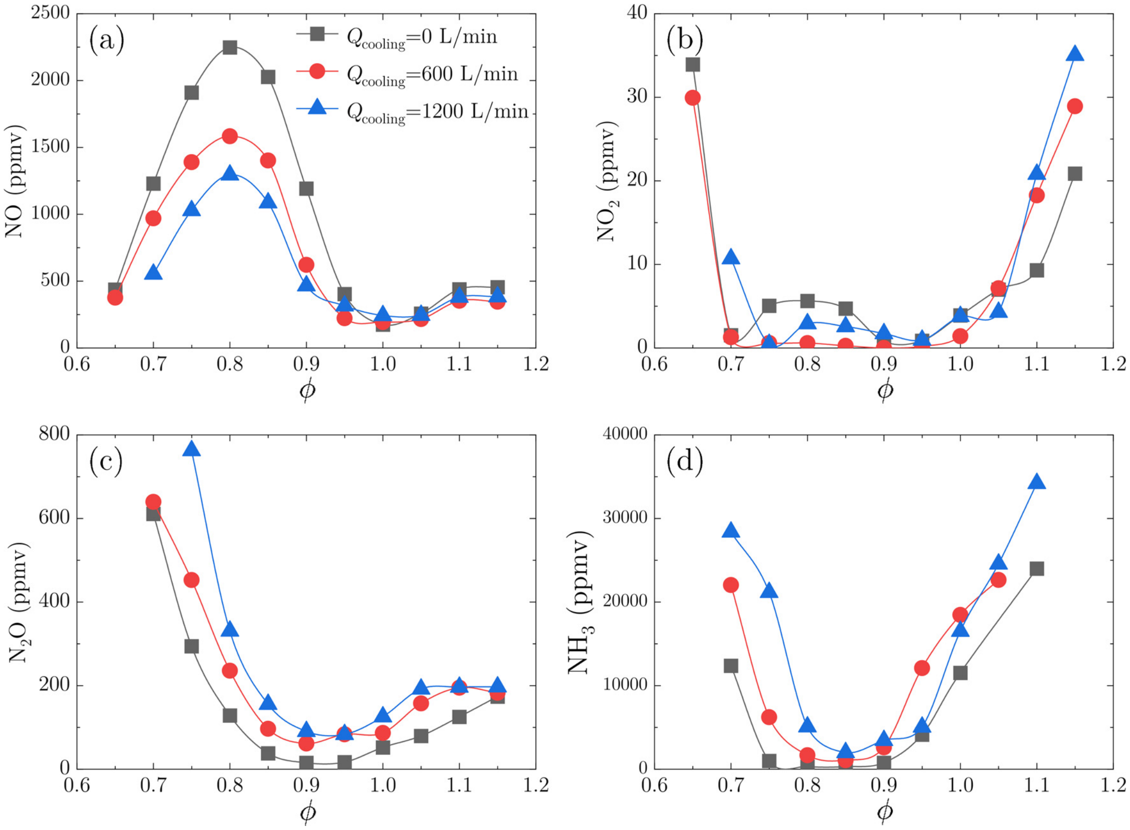

Fig. 8. The effect of the cooling air flow rate $Q_{cooling}$ on the emission characteristics of NO, NO_2, N_2O and NH_3.

served when the air cooling was applied. Therefore, another reason for the decreased NO emission might be attributed to the enhancement on NO reduction in the exhaust gas by the unburned NH_3. For rich conditions, the air cooling shows very limited effect, which agrees with the NO-PLIF measurement. From our previous research [25], $\phi = 1.05$ was the optimal operating condition where the sum of NO and NH_3 emission reached a minimal value for NH_3/air swirling flame. Higher NO was observed as the equivalence ratio goes either lean or rich side. With the increase effect of air cooling, the global NO emission at fuel-lean condition decreases while the general behaviour is preserved. NO_2 is another component of NOx, which exhibits very low value (below 35 ppm) comparing to NO, see Fig. 8(b). In equivalence ratio of 0.7–1.0, it shows single digits which is nearly out of the measurement accuracy of FTIR. Therefore, the behaviour of NO_2 within $\phi = 0.7$–1.0 for different cases may not be caused by its production or consumption mechanism.

One important goal applying NH_3 combustion is to decrease the greenhouse gas. N_2O, a more serious greenhouse gas [42], shows considerable increases within the entire measuring range when the air cooling on the combustion chamber wall was applied, as shown in Fig. 8(c). The enhancement is more significant at fuel lean condition. For example, at $\phi = 0.7$, N_2O increases from to 294 ppm to 780 ppm when $Q_{cooling}$ is increased from 0 to 1200 L/min. By

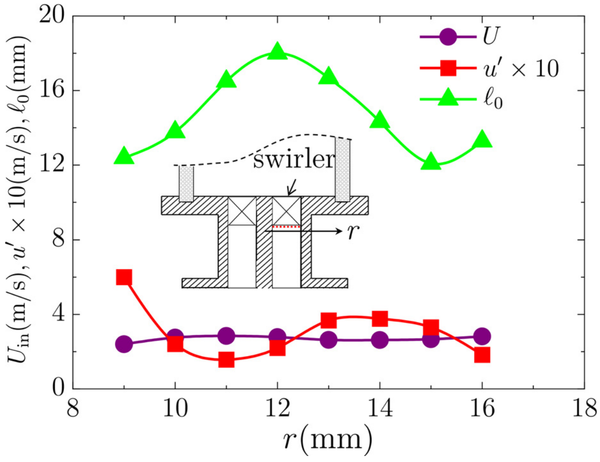

Fig. 9. The turbulence boundary applied in LES. U_{in}, u' and ℓ_0 are the mean axis velocity, turbulence intensity and the integral scale. The measuring positions are indicated in the inset.

observing Fig. 8, N_2O reached a comparable level (i.e., 780 ppm) as NO (i.e., 1000 ppm) at the operating condition of $Q_{\text{cooling}} = 1200$ L/min. From the analysis of chemical reaction pathway, the N_2O can be decomposed through reaction with H radicals at high temperature region. In addition, the rate of NO reduction to N_2O is promoted at the temperature which is lower than the temperature of N_2O decomposition. Therefore, when the local temperature is decreased, large N_2O is produced while the consumption of N_2O decreases, resulting in considerable N_2O emission. The high N_2O may need further treatment in gas turbine combustor.

By comparing the global emissions and the OH-/NO-PLIF measurement results, the first conclusion is that the effect of wall cooling is non-negligible on the N_2O and NOx characteristics. Further analysis on NO profile shows that NO is mainly influenced at near wall region, which means that the thermal effect only in this small region changes the global emission features. Therefore, the current study suggests that the combustor wall cooling employed to reduce thermal stress on combustor liners may have strong effects on the combustion efficiency and emission characteristics in ammonia fuelled gas turbines.

3.4. Large eddy simulation investigation

3.4.1. Validation of numerical results

To further investigate the heat loss on the NOx emission characteristics of NH_3/air flame, LES with detailed chemistry was performed for $\phi = 0.8$ at $U_{\text{in}} = 3$ m/s. In LES, the heat loss conditions were simulated by applying the isothermal wall boundary condition at chamber side walls. The temperature profiles were taken as the fitting curves from experimental data for the case of $U_{\text{in}} = 3$ m/s. In addition, to capture the flame features, the turbulence parameters of the flow boundary at the inlet of computational domain (ahead of swriler) were measured during experiments by a hot-wire anemometer (Dantec, Streamline 90 N). Figure 9 shows the profiles of mean inlet velocity U_{in}, turbulence intensity u' and integral scale ℓ_0 applied at the swirler inlet. It can be seen that the mean inlet velocity is about 3 m/s and the relative turbulence intensity is about 10%.

The comparison of instantaneous and mean 2D NO profile between the experimental and simulation results is shown in Fig. 10. The flame structure obtained by simulation is characterized by the mean NO mass fraction. It can be seen that for both numerical and experimental results, NO mainly exists in the inner recirculation zone (IRZ) of the flame, and the NO distribution presents a V-shaped structure. No NO was observed in the outer recirculation zone (ORZ) which means the NH_3 flame could not be stabilized near the combustion wall under this condition. Both the simulation and experimental results show a contraction phenomenon at the position $z > 45$ mm when heat loss was considered. In all, both instantaneous and mean PLIF images show a good agreement between the numerical and experimental results, indicating a good ability in capturing the flame macro structure and NO species.

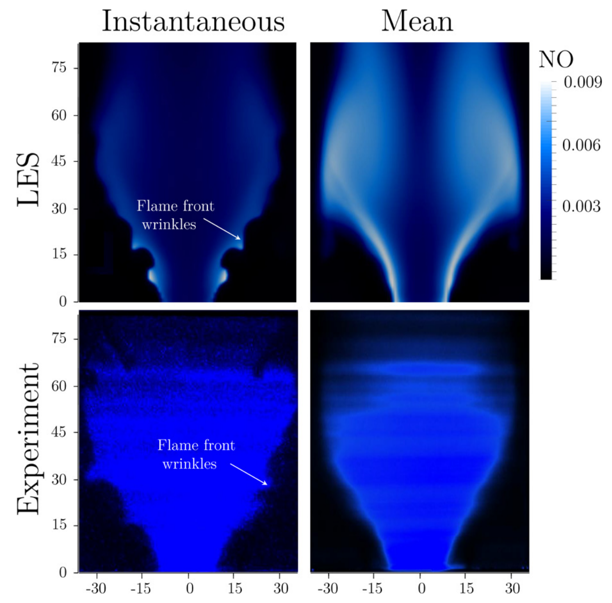

Fig. 10. Comparison of the instantaneous and mean NO radial profile between LES (at $Q_{\text{cooling}} = 0$ L/min, upper panel) and experiments (lower panel). The flame was operated at $\phi = 0.8$ and $U_{\text{in}} = 3$ m/s for NH_3/air flame.

Figure 11 compares the mean and root mean square (r.m.s) of the axial and azimuth velocities of NH_3/air flame at $\phi = 0.8$ and $U = 3$ m/s at different downstream positions. In general, the LES results agrees well with the PIV results and a slight difference could only be seen at the lower position ($z = 10$ mm) around the shear layer for the mean velocity profile. This is mainly due to the strong velocity gradient near the shear layer where the flame surface is artificially thickened. This has a certain influence on the prediction of the velocity. We carefully tested the current mesh by further refining the mesh and found that the refinement did not affect the statistics of the flow field. Overall, the current LES exhibits a good prediction capability on the chemistry, flow dynamics and the proper specifications of the flow thermal boundary conditions.

3.4.2. Discussions on LES results

Figure 12 shows the instantaneous mass fraction of NO, NH_3, N_2O as well as the temperature field of $\phi = 0.8$ at the center plane ($x = 0$ mm) for the adiabatic wall and isothermal wall using the temperature of $Q_{\text{cooling}} = 0$, 200 and 600 L/min. Figure 13 plots the radial distribution of the corresponding species and temperature within 15 mm $< x <$ 35 mm at downstream location of $z = 40$ mm. The effect of wall heat loss on the flame structure, NOx production as well as unburned NH_3 can be clearly observed. An “M” shape flame is observed for the adiabatic condition and “V” shape flames are seen for the flames with isothermal wall conditions, which are also verified experimentally [3]. When the air cooling was introduced, as shown in Fig. 12(a), the flame tends to be lower and the mean temperature within the chamber is decreased. Compared with the flame of adiabatic condition, the temperature is largely decreased in ORZ and near-wall region for the case of $Q_{\text{cooling}} = 0$ L/min, see Fig. 12(a). The region with minus gradient of temperature from chamber axis to wall can be defined as the thermal

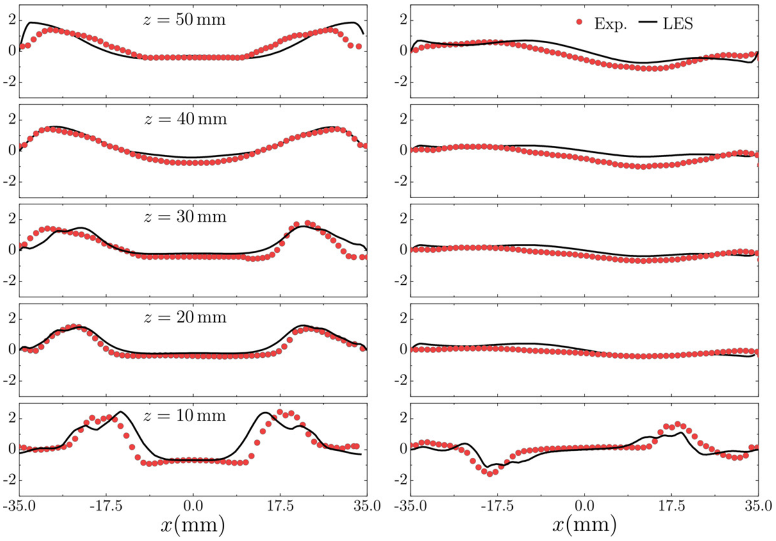

(a) U_z mean (b) U_x mean

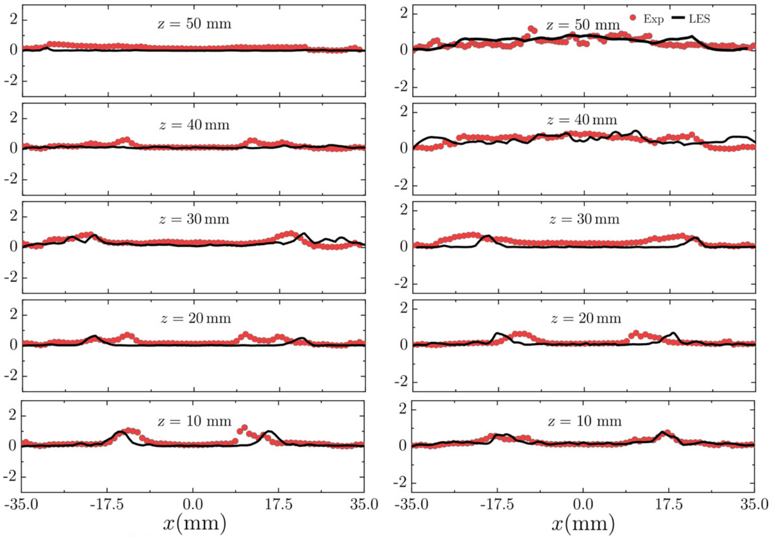

(c) U_z r.m.s (d) U_x r.m.s

Fig. 11. Comparison of the radial profiles of mean and root mean square of axial and azimuthal velocity between LES and PIV measurements. The flame was operated as NH_3/air flame at $\phi = 0.8$ and $U = 3$ m/s at $Q_{cooling} = 0$ L/min. Line: numerical results; symbols: experimental measurements.

boundary layer, as indicated in the figure, where local quenching may occur due to the lower temperature. The existing of the thermal boundary layer is accompanied by an obvious unburned NH_3 region, as shown in Fig. 12(c). Strong NO intensity is seen in the post flame region including the ORZ for the adiabatic condition, since NO spread over the preheat zone and post reaction zone. In comparison, a clear decrease of NO mass fraction is observed in ORZ and thermal boundary layer when $Q_{cooling} = 0$ L/min. It can be considered that NO_2 are barely affected by the heat loss due to its low concentration as showed in Fig. 13(c).

It can be seen from Fig. 13(e) that the thermal boundary layer is getting thicker by increasing $Q_{cooling}$. This leads to an increasing thickness of the unburned NH_3 region as plotted in Fig. 13(d), which results in larger possibility of local quenching and lower combustion efficiency in this region. Moreover, NO is further decreased within an extended region for larger $Q_{cooling}$, as shown in Fig. 13(a). By analyzing the NH_3 consumption pathway, as shown in Fig. 14, it can be seen that that NH_3 undergoes a series of dehydrogenation reactions to generate NO. These reactions are carried out through the NH_3 oxidation by O, H and OH radicals, in which NH3 + OH = H2O + NH2 shows a dominated effect. The temperature decreasing at near wall region caused by wall heat loss may hinder chain branching reaction H+O2= OH+O which is very sensitive to temperature. The combined effect of the two reactions above reduces the NH_3 consumption and combustion efficiency.

To further analyze the contribution of the detailed chemical reactions on NO species, 9 important reactions directly related to NO were found through sensitivity analysis, which are shown below.

$NH + NO = H + N_2O$ (R85)
$HNO + O_2 = HO_2 + NO$ (R148)
$HNO + NH_2 = NH_3 + NO$ (R149)
$NH_2 + NO = NNH + OH$ (R77)
$NH_2 + NO = H_2O + N_2$ (R76)
$H + HNO = H_2 + NO$ (R144)
$N + O_2 = NO + O$ (R90)
$HNO = H + NO$ (R143)
$NH + O = H + NO$ (R79)

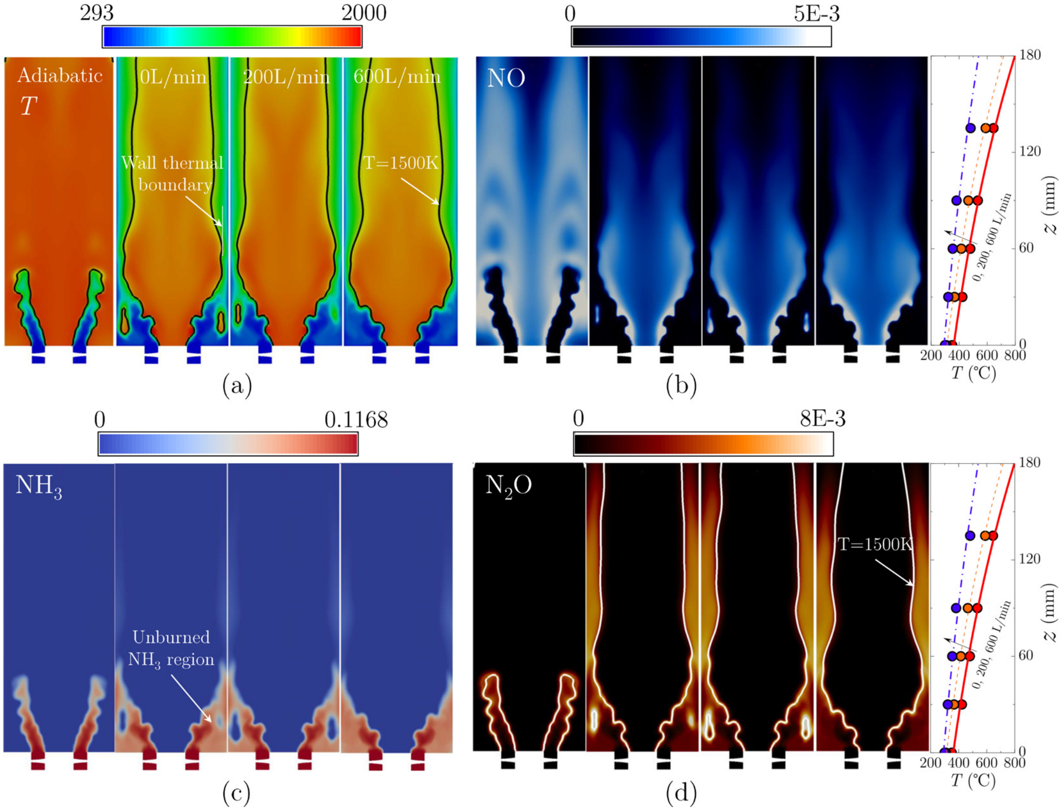

Fig. 12. The instantaneous mass concentration of NO, NH_3, N_2O and the temperature field obtained by LES at $x = 0$ mm. The adiabatic wall and wall temperature of $Q_{\text{cooling}} = 0$, 200 and 600 L/min at $\phi = 0.8$ were applied as the thermal boundaries which were plotted in the right side. The symbols represent the experiment measurement and the lines is the fitting curve. The iso-thermal contour of $T = 1500$ K was plotted on the T and N_2O field.

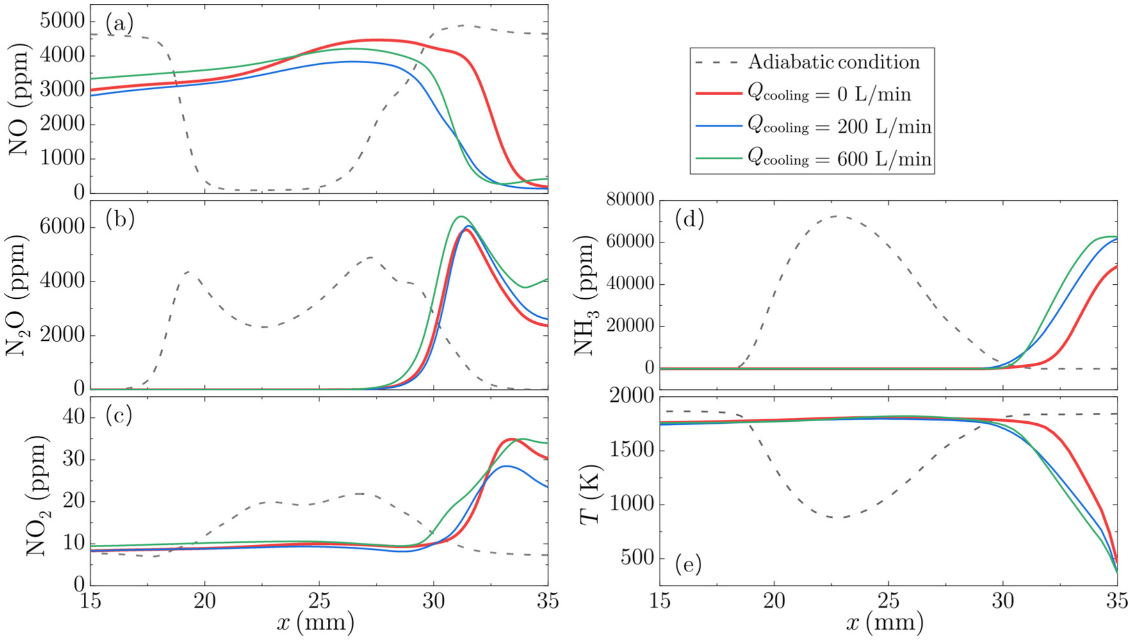

Fig. 13. The air cooling effect on the radial distribution of NO, N_2O, NH_3 and temperature of $\phi = 0.8$ at downstream location of $z = 40$ mm. The unit of the species shown above were transferred to ppm.

In above reactions, R85, R77 and R76 consume NO and the others produce NO. Local species concentration can be affected by mixing, diffusion as well as transportation, which further influences the local chemical reaction rate. Therefore, the coupled reaction rate calculation tool was used to obtain local reaction rate in three-dimensional space. Figure 15(a) shows the effect of heat loss on the NO rate of production within 25 mm $< x <$ 35 mm at $z = 40$ mm. The rate of production of NO (ROP of NO) was obtained by the sum of production and consumption as ROP of NO $= \Sigma|\omega_{\text{pro}}| - \Sigma|\omega_{\text{con}}|$. Positive value means a net NO production and negative value means a net NO consumption. It can be seen that the ROP of NO is decreasing and the peak value moves towards

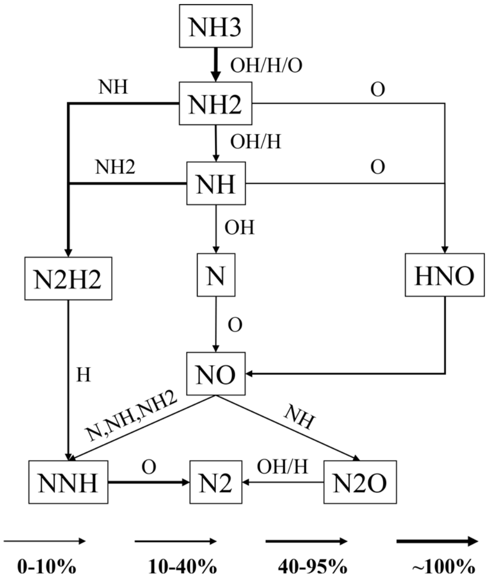

Fig. 14. Reaction pathway analysis, calculated by zero-dimensional reactor with CHEMKIN-pro.

chamber wall by increasing Q_{cooling}. The chemical reaction proportion which is obtained by:

$$\text{Reaction proportion} = \frac{\Sigma|\omega_{\text{pro}}|(\Sigma|\omega_{\text{pro}}|)}{\Sigma|\omega_{\text{pro}}| + \Sigma|\omega_{\text{pro}}|} \tag{13}$$

Figure 15(b) demonstrates the contribution of NO production or consumption in the total chemical reactions near the wall (x = 25~35 mm). In addition, as shown in Fig. 15(b), the contributions of NO consumption and production exhibit a trade-off behaviour near the wall. This further proves that the chemical reactions at near all region determine the global NO emission for the current combustor.

Figure 16 shows the contribution of each reactions to NO production. P_i represents the percentage of ith reaction rate in the total rates of the 9 reactions listed above, which was calculated by

$$P_i = \frac{\omega_{i,\max}}{\Sigma|\omega_{i,\max}|}, \tag{14}$$

where $\omega_{i,max}$ is the maximum value of the ith reaction rate profile within 25 mm $< x <$ 35 mm. It can be seen that heat loss promotes NO consumption by enhancing NH_2+NO = H_2O+N_2 (R76) and NH+NO = H+N_2O (R85). However, the HNO and NH pathway of NH+O = H+NO (R79) and HNO = H+NO (R143), which contribute the most on NO production, are suppressed by heat loss. This indicates that heat loss mainly reduces the fuel NO and the NO emission still mainly comes from the fuel NO for pure NH_3/air flames.

By surveying Fig. 12(d), large N_2O is produced in ORZ and near-wall region due to heat loss. For the adiabatic condition, N_2O is mainly produced at flame front location and tends to be transported to the unburned region (low temperature region). In comparison, N_2O distribution is extended to the burner outlet along the near wall region when heat loss was introduced. In addition, as indicated in Fig. 13(b), N_2O shows a clear increase at near wall region when the heat loss is larger. Results of Ref. [40] show that N_2O and NNH have a special relationship and constructed an important part of NOx mechanism for H_2/air flame with NNH+O = N_2O+H. As the pathway demonstrated in Fig. 14, N_2 blocks the pathway between NNH and N_2O which is much different with H_2/air flame. According to 0D chemical reaction analysis, the two most important chemical reactions affecting the N_2O production are NH+NO = H+N_2O and NH_2+NO = N_2O+N_2 [43]. The consumption of N_2O species is mainly caused by the thermal decomposition of N_2O through the reaction N2O+H = N_2+OH, which mainly occurs under the temperature above 1500 K. For the adiabatic condition, N_2O is quickly consumed due to its thermal decomposition in the burned zone where the temperature is high. When the temperature is lower than 1500 K, N_2O decomposition is largely suppressed due to the low H radical concentration, caused by the decreasing rate of NH_3 dehydrogenation. Therefore, N_2O can be observed in the outer recirculation zone as well as the near wall region (thermal boundary) where the temperature is relatively low. Comparing N_2O with the temperature field, it can be seen that N_2O is mainly observed within the region where the temperature is below 1500 K.

Figure 17 shows the comparison of the mean NO and N_2O emissions at chamber outlet plane obtained from LES and the global emission values measured by FTIR at $\phi = 0.8$. The results of the adiabatic condition are marked by the stars. The LES data was averaged in the outlet plane with the time duration of over 20 ms. Therefore, it can be viewed as the global emission values for the LES, which can be comparable with experimental data. Compared with the adiabatic condition, a significant decrease is observed for NO emission and a clear increase is seen for N_2O emission for the condition of Q_{cooling} = 0 L/min. The NO emission is further decreased and N_2O is further increased when the air cooling effect is strengthened (increasing Q_{cooling}), which shows the consistent behaviour as the experimental findings. According to Fig. 17, NO and N_2O seems to show comparative contributions to the emissions when heat loss is high. By surveying the N_2O mechanism,

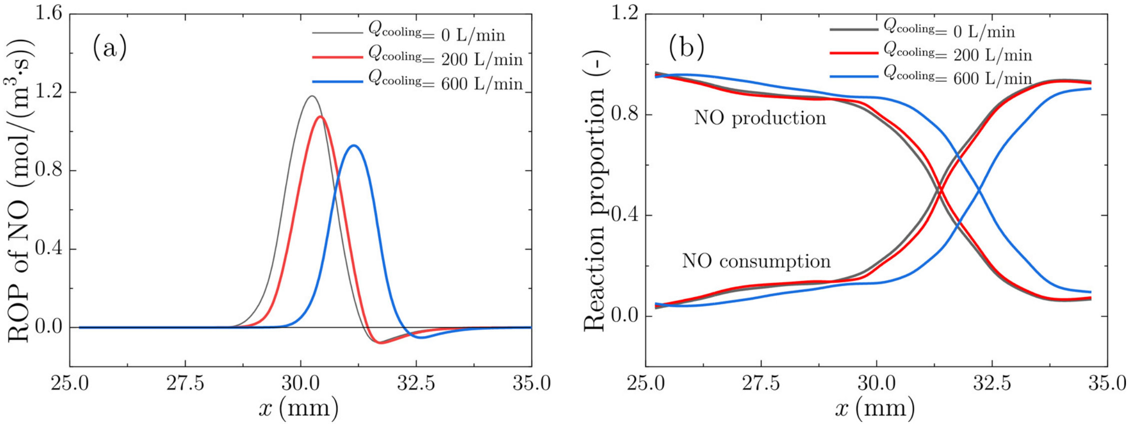

Fig. 15. The chemical reaction at near wall region at z = 40 mm and ϕ = 0.8. (a) The rate of production of NO; (b) the chemical reaction proportion of NO production and consumption.

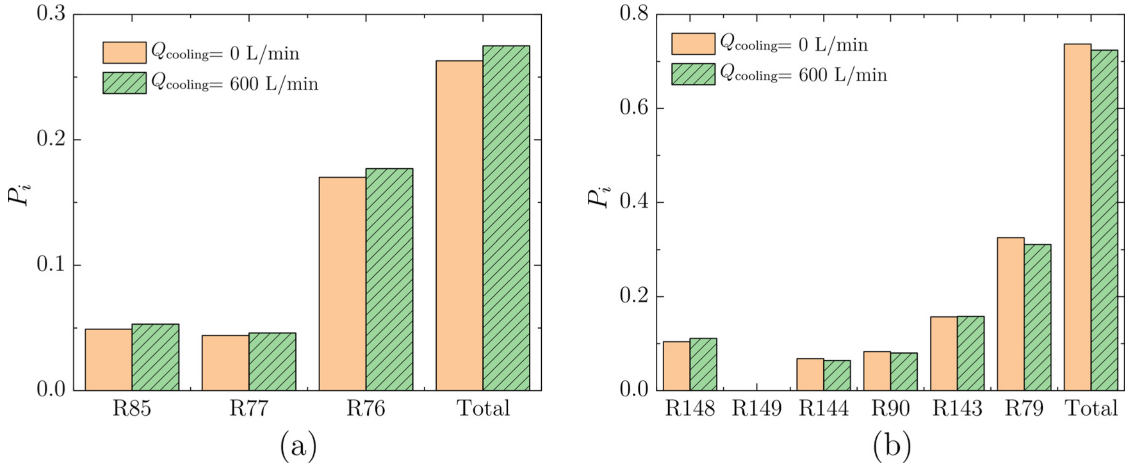

Fig. 16. The influence of heat loss on the main reaction rates related to NO species. The data was obtained at $z = 40$ mm and ϕ =0.8.

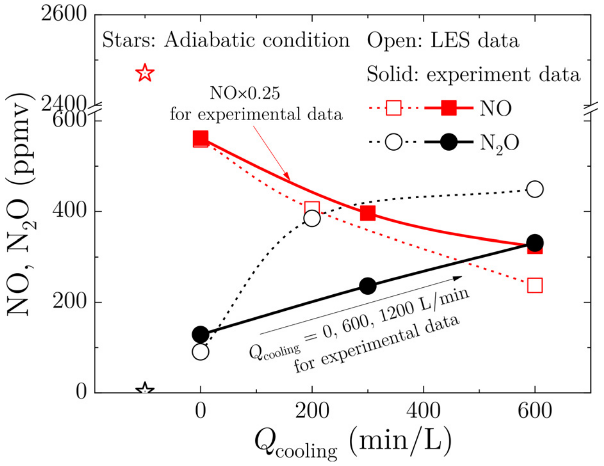

Fig. 17. The comparison of the mean NO (red) and N_2O (black) emissions at chamber outlet obtained from LES and the global emission values measured by FTIR at $\phi = 0.8$. The stars marked the adiabatic condition. Open and solid and symbols represent LES and experimental data. The cooling air flow rates Q_{cooling} were 0, 600 and 1200 L/min for the experiments. The NO emission measured by experiments in the figure was multiplied by 0.25. (For interpretation of the references to colour in this figure legend, the reader is referred to the web version of this article.)

N_2O relates closely to the local temperature as discussed in earlier section. Thus, the accuracy of wall temperature or the heat loss setting at chamber side walls directly decides the prediction ability. Moreover, to further improve the N_2O prediction, a better chemical mechanism which has accurate reactions on N_2O is also needed.

The experimental and numerical data demonstrate that the flame wall heat release greatly affect the thermal boundary near the wall, which affects the local combustion efficiency and the NO/N_2O production in NH_3/air swirling flames. The results also suggests the thermal effect of flame-wall interaction on the NOx production and combustion efficiency should be fully considered when designing the gas turbine combustion chamber with strong wall cooling, since N_2O might become a more serious emission in NH_3 fuelled gas turbines.

4. Conclusions

This study is motivated by the strong thermal effect (wall heat loss effect) of NH_3/air flame resulted from its low reactivity and high NOx emission. The thermal effect was investigated in a swirling combustion chamber with air film cooling. For the current chamber, the convection wall heat loss is getting larger as the cooling air flow rate Q_{cooling} increases. For lean conditions ($\phi = 0.8$), the global NOx emissions are largely affected by the heat loss. The flame front, indicated by NO profile, tends to be relatively farther from the combustor wall and the flame is more fragmentized by increasing Q_{cooling}, which means a larger possibility of local quenching at near wall region. Global NO emission measured by FTIR significantly decreases when the heat loss is enhanced. The primary reason is the decreased combustion efficiency of NH_3 at near wall region. Secondly, NO production from HNO and NH pathway is hindered the due to the local decreased OH. Lastly, the larger unburned NH_3 in the exhausted gas may also consumes NO by the NO reduction reactions. N_2O, a more serious greenhouse gas than CO_2, reaches a comparable value as NO emissions as the heat loss increases, which is mainly due to suppression on N_2O decomposition and the promotion of N_2O production from NO at near wall region. In comparison, the influences of heat loss are limited at stoichiometric and rich conditions. The results of this investigation imply that N_2O might become a more serious emission component in NH_3 fuelled gas turbines. This study also suggests that the NOx production in thermal boundary maybe a key factor in low NOx combustion chamber design.

Declaration of Competing Interest

The authors declare that they have no conflict of interest.

Acknowledgements

This study is supported by the National Natural Science Foundation of China (No. 52176130).

References

[1] H. Kobayashi, A. Hayakawa, K.K.A. Somarathne, E.C. Okafor, Science and technology of ammonia combustion, Proc. Combust Inst. 37 (1) (2019) 109–133.
[2] A. Valera-Medina, H. Xiao, M. Owen-Jones, W. David, P. Bowen, Ammonia for power, Prog. Energy Combust. Sci. 69 (2018) 63–102.
[3] M. Zhang, X. Wei, J. Wang, Z. Huang, H. Tan, The blow-off and transient characteristics of co-firing ammonia/methane fuels in a swirl combustor, Proc. Combust. Inst. 38 (4) (2021) 5181–5190.
[4] A.A. Khateeb, T.F. Guiberti, G. Wang, W.R. Boyette, M. Younes, A. Jamal, W.L. Roberts, Stability limits and no emissions of premixed swirl ammonia-air flames enriched with hydrogen or methane at elevated pressures, Int. J. Hydrogen Energy 46 (21) (2021) 11969–11981.
[5] A. Hayakawa, Y. Arakawa, R. Mimoto, K.K.A. Somarathne, T. Kudo, H. Kobayashi, Experimental investigation of stabilization and emission characteristics of ammonia/air premixed flames in a swirl combustor, Int. J. Hydrogen Energy 42

(19) (2017) 14010–14018. Special Issue on The 21st World Hydrogen Energy Conference (WHEC 2016), 13-16 June 2016, Zaragoza, Spain

[6] E.C. Okafor, K.K.A. Somarathne, A. Hayakawa, T. Kudo, O. Kurata, N. Iki, H. Kobayashi, Towards the development of an efficient low-NOx ammonia combustor for a micro gas turbine, Proc. Combust. Inst. 37 (4) (2019) 4597–4606.

[7] A. Hayakawa, T. Goto, R. Mimoto, Y. Arakawa, T. Kudo, H. Kobayashi, Laminar burning velocity and markstein length of ammonia/air premixed flames at various pressures, Fuel 159 (2015) 98–106.

[8] X. Han, Z. Wang, Y. He, Y. Liu, Y. Zhu, A.A. Konnov, The temperature dependence of the laminar burning velocity and superadiabatic flame temperature phenomenon for NH_3/air flames, Combust. Flame 217 (2020) 314–320.

[9] A. Hayakawa, T. Goto, R. Mimoto, T. Kudo, H. Kobayashi, NO formation/reduction mechanisms of ammonia/air premixed flames at various equivalence ratios and pressures, Mech. Eng. J. 2 (1) (2015) 14-00402.

[10] H. Nakamura, M. Shindo, Effects of radiation heat loss on laminar premixed ammonia/air flames, Proc. Combust. Inst. 37 (2) (2019) 1741–1748.

[11] A. Hayakawa, Y. Hirano, E.C. Okafor, H. Yamashita, T. Kudo, H. Kobayashi, Experimental and numerical study of product gas characteristics of ammonia/air premixed laminar flames stabilized in a stagnation flow, Proc. Combust. Inst. 38 (2) (2021) 2409–2417.

[12] Y. Huang, V. Yang, Dynamics and stability of lean-premixed swirl-stabilized combustion, Prog. Energy Combust. Sci. 35 (4) (2009) 293–364.

[13] T. Guiberti, D. Durox, P. Scouflaire, T. Schuller, Impact of heat loss and hydrogen enrichment on the shape of confined swirling flames, Proc. Combust. Inst. 35 (2) (2015) 1385–1392.

[14] F. Verkamp, M. Hardin, J. Williams, Ammonia combustion properties and performance in gas-turbine burners, Symp. (Int.) Combust. 11 (1) (1967) 985–992.

[15] T.F. Guiberti, M. Belhi, J.S. Damazo, E. Kwon, W.L. Roberts, D.A. Lacoste, Quenching distance of laminar methane-air flames at cryogenic temperatures and implications for flame arrester design, Appl. Energy Combust. Sci. 1–4 (2020) 100001.

[16] A. Valera-Medina, R. Marsh, J. Runyon, D. Pugh, P. Beasley, T. Hughes, P. Bowen, Ammonia–methane combustion in tangential swirl burners for gas turbine power generation, Appl. Energy 185 (2017) 1362–1371. Clean, Efficient and Affordable Energy for a Sustainable Future

[17] E.C. Okafor, M. Tsukamoto, A. Hayakawa, K.K.A. Somarathne, T. Kudo, T. Tsujimura, H. Kobayashi, Influence of wall heat loss on the emission characteristics of premixed ammonia-air swirling flames interacting with the combustor wall, Proc. Combust. Inst. 38 (4) (2021) 5139–5146.

[18] X. Wei, M. Zhang, Z. An, J. Wang, Z. Huang, H. Tan, Large eddy simulation on flame topologies and the blow-off characteristics of ammonia/air flame in a model gas turbine combustor, Fuel 298 (2021) 120846.

[19] M. Lee, Y. Fan, Y. Ju, Y. Suzuki, Ignition characteristics of premixed cool flames on a heated wall, Combust. Flame 231 (2021) 111476.

[20] A. Hayakawa, M. Hayashi, M. Kovaleva, G.J. Gotama, E.C. Okafor, S. Colson, S. Mashruk, A. Valera-Medina, T. Kudo, H. Kobayashi, Experimental and numerical study of product gas and N_2O emission characteristics of ammonia/hydrogen/air premixed laminar flames stabilized in a stagnation flow, Proc. Combust. Inst. 39 (2) (2023) 1625–1633.

[21] K.D.K.A. Somarathne, E. C. Okafor, A. Hayakawa, T. Kudo, O. Kurata, N. Iki, H. Kobayashi, Emission characteristics of turbulent non-premixed ammonia/air and methane/air swirl flames through a rich-lean combustor under various wall thermal boundary conditions at high pressure, Combust. Flame 210 (2019) 247–261.

[22] S. Mashruk, M. Kovaleva, A. Alnasif, C.T. Chong, A. Hayakawa, E.C. Okafor, A. Valera-Medina, Nitrogen oxide emissions analyses in ammonia/hydrogen/air premixed swirling flames, Energy 260 (2022) 125183.

[23] S. Mashruk, M. Vigueras-Zuniga, M.T. del Cueto, H. Xiao, C. Yu, U. Maas, A. Valera-Medina, Combustion features of $CH_4/NH_3/H_2$ ternary blends, Int. J. Hydrogen Energy 47 (70) (2022) 30315–30327. XXI International Meeting of the Mexican Hydrogen Society

[24] X. Wei, M. Zhang, J. Wang, Z. Huang, Investigation on lean blow-off characteristics and stabilization mechanism of premixed hydrogen enhanced ammonia/air swirl flames in a gas turbine combustor, Combust. Flame 249 (2023) 112600.

[25] M. Zhang, Z. An, X. Wei, J. Wang, Z. Huang, H. Tan, Emission analysis of the CH_4/NH_3/air co-firing fuels in a model combustor, Fuel 291 (2021) 120135.

[26] M. Zhang, Z. An, L. Wang, X. Wei, B. Jianayihan, J. Wang, Z. Huang, H. Tan, The regulation effect of methane and hydrogen on the emission characteristics of ammonia/air combustion in a model combustor, Int. J. Hydrogen Energy 46 (40) (2021) 21013–21025.

[27] S. Guo, J. Wang, W. Zhang, B. Lin, Y. Wu, S. Yu, G. Li, Z. Hu, Z. Huang, Investigation on bluff-body and swirl stabilized flames near lean blowoff with PIV/PLIF measurements and LES modelling, App. Therm. Eng. 160 (2019) 114021.

[28] F. Charlette, C. Meneveau, D. Veynante, A power-law flame wrinkling model for LES of premixed turbulent combustion part II: dynamic formulation, Combust. Flame 131 (2002) 181–197.

[29] W. Han, H. Wang, G. Kuenne, E.R. Hawkes, J.H. Chen, J. Janicka, C. Hasse, Large eddy simulation/dynamic thickened flame modeling of a high Karlovitz number turbulent premixed jet flame, Proc. Combust. Inst. 37 (2019) 2555–2563.

[30] S. Guo, J. Wang, X. Wei, S. Yu, M. Zhang, Z. Huang, Numerical simulation of premixed combustion using the modified dynamic thickened flame model coupled with multi-step reaction mechanism, Fuel 233 (2018) 346–353.

[31] J. Jarosinski, The thickness of laminar flames, Combus. Flame 56 (3) (1984) 337–342.

[32] G. Wang, M. Boileau, D. Veynante, K. Truffin, Large eddy simulation of a growing turbulent premixed flame kernel using a dynamic flame surface density model, Combust. Flame 159 (2012) 2742–2754.

[33] G. Wang, M. Boileau, D. Veynante, Implementation of a dynamic thickened flame model for large eddy simulations of turbulent premixed combustion, Combust. Flame 158 (2011) 2199–2213.

[34] M. Zhang, J. Wang, Y. Xie, Z. Wei, W. Jin, Z. Huang, H. Kobayashi, Measurement on instantaneous flame front structure of turbulent premixed CH_4/H_2/air flames, Exp. Therm. Fluid Sci. 52 (2014) 288–296.

[35] CHEMKIN-PRO 17.2, ANSYS, Inc.: San Diego(2016).

[36] A. Stagni, C. Cavallotti, S. Arunthanayothin, Y. Song, O. Herbinet, F. Battin-Leclerc, T. Faravelli, An experimental, theoretical and kinetic-modeling study of the gas-phase oxidation of ammonia, React. Chem. Eng. 5 (2020) 696–711.

[37] J.P. Holman, Heat Transfer, Mcgraw-Hill, New York, 2010.

[38] D. Staton, A. Cavagnino, Convection heat transfer and flow calculations suitable for electric machines thermal models, Ind. Electron., IEEE Trans. 55 (2008) 3509–3516.

[39] P. Agostinelli, D. Laera, I. Boxx, L. Gicquel, T. Poinsot, Impact of wall heat transfer in large eddy simulation of flame dynamics in a swirled combustion chamber, Combust. Flame 234 (2021) 111728.

[40] T. Capurso, D. Laera, E. Riber, B. Cuenot, NOx pathways in lean partially premixed swirling H_2-air turbulent flame, Combust. Flame 248 (2023) 112581.

[41] M. Zhang, J. Wang, J. Wu, Z. Wei, Z. Huang, H. Kobayashi, Flame front structure of turbulent premixed flames of syngas oxyfuel mixtures, Int. J. Hydrog Energy 39 (10) (2014) 5176–5185.

[42] H. Tian, R. Xu, J.G. Canadell, R.L. Thompson, Y. Yao, A comprehensive quantification of global nitrous oxide sources and sinks, Nature 586 (7828) (2020) 248–256.

[43] R. Lindstedt, F. Lockwood, M. SeLIM, Detailed kinetic modelling of chemistry and temperature effects on ammonia oxidation, Combust. Sci. Tech. 99 (4–6) (1994) 253–276.